

Cascaded-ring-resonator-loaded Mach–Zehnder modulator for enhanced modulation efficiency in wide optical bandwidth

Suguru Akiyama,^{1,2,*} Teruo Kurahashi,¹ Ken Morito,¹ Tsuyoshi Yamamoto,¹ Tatsuya Usuki,¹ and Shintaro Nomura²

¹Fujitsu Laboratories Ltd. 10-1 Morinosato-Wakamiya, 243-0122, Japan

²Graduate School of Pure and Applied Sciences, University of Tsukuba, 1-1-1 Tennoudai, Tsukuba 305-8571, Japan

*akiyama.suguru@jp.fujitsu.com

Abstract: A cascaded-ring-resonator-loaded Mach–Zehnder modulator (CRR-MZM) is presented in which a number of cascaded ring resonators (RRs) are loaded in the interferometer as phase modulators. The ability of the design to provide enhanced modulation efficiency at a wide optical bandwidth is demonstrated in comparison with a conventional single-RR-type modulator without an interferometer. The optimization of RRs for the CRR-MZM is investigated experimentally by measuring the transmission spectra in both intensity and group delay of RRs having various structural parameters. Using the optimized parameters, we fabricated a CRR-MZM with 10 cascaded RRs loaded on each arm of the interferometer on a silicon-on-insulate substrate. The RRs had pin-diodes along the waveguides, which were operated with forward bias voltage. Its modulation efficiency was enhanced by a factor of 4.4 at the expense of additional loss of less than 3.5 dB compared with a standard non-resonant MZM. 10 Gb/s-operations of CRR-MZM were successfully demonstrated using pre-emphasized RF signals with amplitude of 1.5 V_{pp} in a wavelength range of 2 nm.

©2012 Optical Society of America

OCIS codes: (250.4110) Modulators; (250.7360) Waveguide modulators; (230.5750) Resonators; (250.5300) Photonic integrated circuits.

References and links

1. D. A. B. Miller, "Device requirements for optical interconnects to silicon chips," *Proc. IEEE* **97**(7), 1166–1185 (2009).
2. L. C. Kimmerling, D. Ahn, A. B. Apsel, M. Beals, D. Carothers, Y.-K. Chen, T. Conway, D. M. Gill, M. Grove, C.-Y. Hong, M. Lipson, J. Liu, J. Michel, D. Pan, S. S. Patel, A. T. Pomerene, M. Rasras, D. K. Sparacin, K.-Y. Tu, A. E. White, and C. W. Wong, "Electronic-photonic integrated circuits on the CMOS platform," *Proc. SPIE* **6125**, 612502, 612502-10 (2006).
3. A. Liu, R. Jones, L. Liao, D. Samara-Rubio, D. Rubin, O. Cohen, R. Nicolaescu, and M. Paniccia, "A high-speed silicon optical modulator based on a metal-oxide-semiconductor capacitor," *Nature* **427**(6975), 615–618 (2004).
4. W. M. Green, M. J. Rooks, L. Sekaric, and Y. A. Vlasov, "Ultra-compact, low RF power, 10 Gb/s silicon Mach-Zehnder modulator," *Opt. Express* **15**(25), 17106–17113 (2007).
5. G. T. Reed, G. Mashanovich, F. Y. Gardes, and D. J. Thomson, "Silicon optical modulators," *Nat. Photonics* **4**(8), 518–526 (2010).
6. D. J. Thomson, F. Y. Gardes, J.-M. Fedeli, S. Zlatanovic, Y. Hu, B. P. P. Kuo, E. Myslivets, N. Alic, S. Radic, G. Z. Mashanovich, and G. T. Reed, "50-Gb/s silicon optical modulator," *IEEE Photon. Technol. Lett.* **24**(4), 234–236 (2012).
7. Q. Xu, S. Manipatruni, B. Schmidt, J. Shakya, and M. Lipson, "12.5 Gbit/s carrier-injection-based silicon micro-ring silicon modulators," *Opt. Express* **15**(2), 430–436 (2007).
8. P. Dong, S. Liao, H. Liang, W. Qian, X. Wang, R. Shafiqi, D. Feng, G. Li, X. Zheng, A. V. Krishnamoorthy, and M. Asghari, "High-speed and compact silicon modulator based on a racetrack resonator with a 1 V drive voltage," *Opt. Lett.* **35**(19), 3246–3248 (2010).
9. J. Rosenberg, W. M. Green, A. Ryllyakov, C. Schow, S. Assefa, B. G. Lee, C. Jahnes, and Y. Vlasov, "Ultra-low-voltage micro-ring modulator integrated with a CMOS feed-forward equalization driver," in *Proceedings of Optical Fiber Communication Conference*, OSA Technical Digest (CD) (Optical Society of America, 2011), paper OWQ4.

10. W. D. Sacher, W. M. J. Green, S. Assefa, T. Barwicz, S. M. Shank, Y. A. Vlasov, and J. K. S. Poon, "Controlled coupling in silicon microrings for high-speed, high extinction ratio, and low-chirp modulation," in *Proceedings of Conference on Lasers and Electro-Optics / Quantum Electronics and Laser Science Conference*, OSA Technical Digest (CD) (Optical Society of America, 2011), paper PDPA8.
11. J. C. Rosenberg, W. M. J. Green, S. Assefa, T. Barwicz, M. Yang, S. M. Shank, and Y. A. Vlasov, "Low-power 30 Gbps silicon microring modulator," in *Proceedings of Conference on Lasers and Electro-Optics / Quantum Electronics and Laser Science Conference*, OSA Technical Digest (CD) (Optical Society of America, 2011), paper PDPB9.
12. G. Li, X. Zheng, J. Yao, H. Thacker, I. Shubin, Y. Luo, K. Raj, J. E. Cunningham, and A. V. Krishnamoorthy, "25Gb/s 1V-driving CMOS ring modulator with integrated thermal tuning," *Opt. Express* **19**(21), 20435–20443 (2011).
13. K. Padmaraju, J. Chan, L. Chen, M. Lipson, and K. Bergman, "Dynamic stabilization of a microring modulator under thermal perturbation," in *Proceedings of Optical Fiber Communication Conference*, OSA Technical Digest (CD) (Optical Society of America, 2012), paper OW4F.2.
14. S. Akiyama, T. Kurahashi, T. Baba, N. Hatori, T. Usuki, and T. Yamamoto, "A 1V peak-to-peak driven 10-Gbps slow-light silicon Mach-Zehnder modulator using cascaded ring resonators," *Appl. Phys. Express* **3**(7), 072202 (2010).
15. D. M. Gill, S. S. Patel, M. Rasras, Kun-Yii Tu, A. E. White, Young-Kai Chen, A. Pomerene, D. Carothers, R. L. Kamocsai, C. M. Hill, and J. Beattie, "CMOS-compatible Si-ring-assisted Mach-Zehnder interferometer with internal bandwidth equalization," *IEEE J. Sel. Top. Quantum Electron.* **16**(1), 45–52 (2010).
16. A. M. Gutierrez, A. Brimont, G. Rasigade, M. Ziebell, D. Marris-Morini, J.-M. Fedeli, L. Vivien, J. Marti, and P. Sanchis, "Ring-assisted Mach-Zehnder interferometer silicon modulator for enhanced performance," *J. Lightwave Technol.* **30**(1), 9–14 (2012).
17. H. C. Nguyen, Y. Sakai, M. Shinkawa, N. Ishikura, and T. Baba, "10 Gb/s operation of photonic crystal silicon optical modulators," *Opt. Express* **19**(14), 13000–13007 (2011).
18. A. Brimont, D. J. Thomson, P. Sanchis, J. Herrera, F. Y. Gardes, J. M. Fedeli, G. T. Reed, and J. Marti, "High speed silicon electro-optical modulators enhanced via slow light propagation," *Opt. Express* **19**(21), 20876–20885 (2011).
19. J. Liu, M. Beals, A. Pomerene, S. Bernardis, R. Sun, J. Cheng, L. C. Kimerling, and J. Michel, "Waveguide-integrated, ultralow-energy GeSi electro-absorption modulators," *Nat. Photonics* **2**(7), 433–437 (2008).
20. R. Ding, T. Baehr-Jones, Y. Liu, R. Bojko, J. Witzens, S. Huang, J. Luo, S. Benight, P. Sullivan, J.-M. Fedeli, M. Fournier, L. Dalton, A. Jen, and M. Hochberg, "Demonstration of a low $V_{\pi}L$ modulator with GHz bandwidth based on electro-optic polymer-clad silicon slot waveguides," *Opt. Express* **18**(15), 15618–15623 (2010).
21. H.-W. Chen, J. D. Peters, and J. E. Bowers, "Forty Gb/s hybrid silicon Mach-Zehnder modulator with low chirp," *Opt. Express* **19**(2), 1455–1460 (2011).
22. R. A. Soref and B. R. Bennett, "Electrooptical effects in silicon," *IEEE J. Quantum Electron.* **23**(1), 123–129 (1987).
23. H. Kaneshige, Y. Ueyama, H. Yamada, T. Arakawa, and Y. Kokubun, "Quantum well Mach-Zehnder modulator with single microring resonator and optimized arm length," in *Proceedings of 17th Microoptics Conference* (Optical Society of Japan, 2011), paper G-5.
24. F. Xia, L. Sekaric, and Y. A. Vlasov, "Ultra-compact optical buffers on a silicon chip," *Nat. Photonics* **1**(1), 65–71 (2007).
25. H. Tazawa, Y. Kuo, I. Dunayevskiy, J. Luo, A. K. Y. Jen, H. Fetterman, and W. Steier, "Ring resonator based electrooptic polymer traveling-wave modulator," *J. Lightwave Technol.* **24**(9), 3514–3519 (2006).
26. A. Yariv, "Universal relations for coupling of optical power between microresonators and dielectric waveguides," *Electron. Lett.* **36**(4), 321–322 (2000).
27. B. E. Little, S. T. Chu, H. A. Haus, J. Foresi, and J.-P. Laine, "Microring resonator channel dropping filters," *J. Lightwave Technol.* **15**(6), 998–1005 (1997).
28. H. F. Taylor, "Enhanced electrooptic modulation efficiency utilizing slow-wave optical propagation," *J. Lightwave Technol.* **17**(10), 1875–1883 (1999).
29. O. Schwelb, "Transmission, group delay, and dispersion in single-ring optical resonators and add/drop filters - a tutorial overview," *J. Lightwave Technol.* **22**(5), 1380–1394 (2004).

1. Introduction

Optical modulators play a key role in optical communication systems by converting high-speed electrical signals, typically 10 Gb/s or even higher, to optical signals. There have been continuous demands on modulators for reduced power consumption and optical insertion loss (IL), and a smaller footprint, to increase transmission capacity of systems at a constant total power consumption and size. In particular, silicon-based modulators with low power consumption and small footprints have become highly desirable since silicon photonics was recognized as an enabling technology for large-scale, high-density optical-interconnects [1,2]. Consequently, silicon modulators have exhibited extraordinary improvements in performance in the past decade [2–21]. In those studies, overcoming the performance limitations caused by

the material properties of silicon has been a major challenge. Unfortunately, silicon lacks a strong electro-optical effect [22], unlike traditional III–V systems.

Employing optical resonators is an effective way of improving the performance of the modulators beyond the material limits because the resonators can enhance the modulation efficiency at the resonant wavelengths [7–18]. In particular, modulators based on a single micro ring resonator (RR) in an all-pass filter (APF) configuration have shown promise [7–13]. They have achieved the lowest driving voltage and highest modulation speed among silicon modulators using resonators. These modulators have sharp dips in the intensity transmission spectrum at the resonant wavelengths. A tiny change in the refractive index according to the electrical input signals causes sufficient intensity variation by shifting the resonant wavelengths; we call this type of modulator a single-ring-resonator-based spectral shifting modulator (SRR-SSM). It is widely recognized that an inherent trade-off exists between the modulation efficiency and the optical bandwidth in which the modulator can operate without any tuning of the resonant wavelengths. An optical bandwidth as small as 0.1 nm was commonly reported for these modulators [7–13]. This narrow operating window made those modulators difficult to use in practical systems without precise dynamic tuning of the resonant wavelengths of the RRs [12,13]. This need for a tuning system could restrict the application of those modulators. The lack of a degree of freedom in design is responsible for this constraint. For a given refractive index change, it is essential to increase the Q value of the resonators, to obtain large modulation efficiency. This inevitably causes a narrow optical bandwidth.

To overcome this limitation, we have proposed and investigated cascaded-ring-resonator-loaded Mach–Zehnder modulators (CRR-MZMs) [14]. Unlike other modulators [15,16,23], ours use more than one cascaded RR in an APF configuration [24] incorporated in a Mach–Zehnder interferometer (MZI). For a given change in the refractive index, it is possible to obtain a large intensity modulation not only by increasing the Q value of the RRs but also by increasing the number of cascaded RRs. By using these two design parameters, the CRR-MZM could perform differently from SRR-SSMs and therefore widen the application range of resonator-based modulators. Nevertheless, few works have been reported that demonstrated the basic operation of CRR-MZMs using RRs that were not necessarily optimized for them [14]. Consequently, the potential performance of CRR-MZMs has not yet been revealed in terms of the modulation efficiency and optical bandwidth.

In this paper, we first describe the design concept of the CRR-MZM using analytic calculations in comparison with SRR-SSM. On the basis of the results, we experimentally investigate the detailed optimization of the structure of the RRs for the CRR-MZMs. We fabricated a CRR-MZM on a silicon-on-insulator substrate using RRs with the optimized parameters. The RRs had pin-diodes along the waveguides, which were operated with forward bias voltage. We measured the fundamental characteristics of the modulator, such as the enhancement factor of the modulation, the wavelength bandwidth, and the optical loss of the RRs. We then conducted high-speed large-signal modulation experiments using the CRR-MZM. We used pre-emphasized signals with amplitude of $1.5 V_{pp}$ to operate the pin-diodes of the RRs with forward bias voltage. We obtained 10-Gb/s operations in a wavelength range of 2 nm, which is about 20 times wider than those reported for SRR-SSMs, while maintaining an enhancement of 4.4 times in the modulation efficiency due to the optical resonance.

2. Device concept

In this section, the design concept of the CRR-MZM is shown by analytical calculations of the modulation efficiency. The difference in design capability between CRR-MZMs and conventional SRR-SSMs is emphasized.

Figure 1 is a schematic view of an SRR-SSM [7–13] and a CRR-MZM [14]; the structural parameters of RRs are also defined. The SRR-SSM has a simple structure consisting of a single RR, whereas the CRR-MZM has a number of cascaded RRs incorporated into an MZI. The RRs in both types of modulators have electrodes on both sides of the waveguide along the ring to apply a voltage to the waveguide. Each RR has two principal parameters that

define its structure: the radius (R), which determines its free spectral range (FSR), and the coupling strength (y) between the ring and the bus waveguide. Here, y is defined so that y^2 is the fraction of the power transmitted in the bus waveguide from one side to the other in the coupling region for a unit incident. Accordingly, a power of $1 - y^2$ is transferred from the bus to the ring waveguide, as shown in Fig. 1(b). The CRR-MZM has one additional parameter, the number of rings (N) cascaded on each arm of the MZI. In our definition, N means the number of RRs connected to single bus waveguide. The CRR-MZM contains $2N$ RRs in total.

For the SRR-SSM, a continuous wave of light with an angular frequency ω and unit amplitude is input from one side of the bus waveguide of the RR, as shown in Fig. 1(a). The output is obtained from the other side of the bus waveguide and has a complex amplitude of T as a function of ω . When a voltage V is applied to the ring waveguide, T changes in both intensity and phase through the change in the refractive index of the ring waveguide. The SRR-SSM uses only a change in the amplitude of T , whereas CRR-MZMs use the phase change of the transmitted light of N cascaded RRs (T^N) by converting it into an intensity change by the MZI.

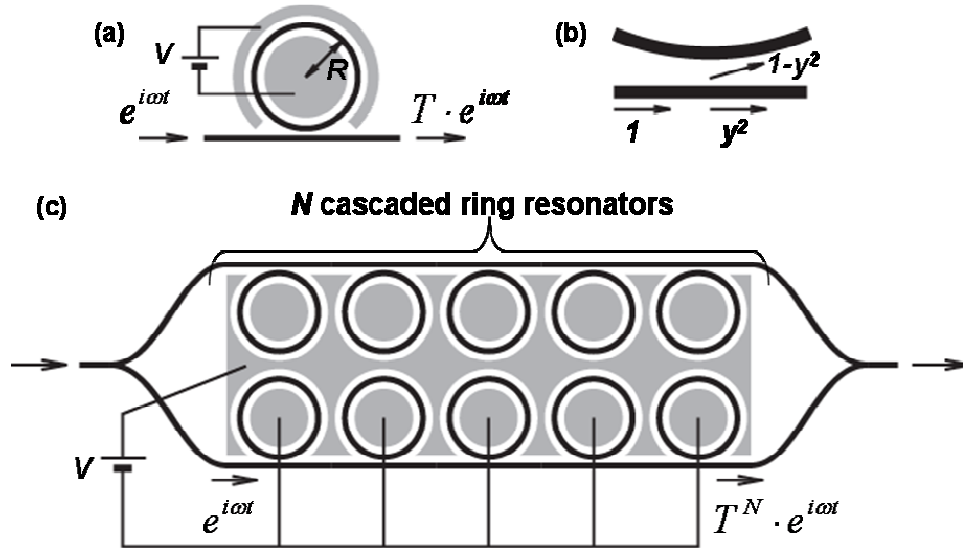


Fig. 1. Schematic view of RR-based modulators and definition of RR parameters. (a) SRR-SSM. (b) Coupling between ring and bus waveguide as a part of RRs. y^2 and $1 - y^2$ indicate the fraction of the power transmitted to the bus and the ring waveguide, respectively. (c) CRR-MZM.

We derived an analytic formula for the modulation efficiency of the RR. Equation (1) is the transfer function of a single RR as a function of ϕ , where ϕ is the round-trip (RT) phase of the RR. α and β are the attenuation and propagation constants of the ring waveguide, respectively [25–27].

$$T(\phi) = \frac{x \cdot e^{-i\phi} - y}{xy \cdot e^{-i\phi} - 1}, \text{ where } x = e^{-\frac{\alpha}{2}(2\pi R)}, \text{ and } \phi = \beta \cdot (2\pi R). \quad (1)$$

In the operation of modulators based on RRs, the voltage V causes a change in the refractive index of the ring waveguide, which in turn induces changes in ϕ and T through a change in the propagation constant β .

2.1 SRR-SSM

The SRR-SSM uses a steep slope of the intensity of the transfer function T . To obtain this transfer function, a condition of critical coupling is typically used, in which T becomes null at

the resonant wavelength [26]. This condition is satisfied when $x = y$ in (1). In this case, the output power of the single RR and its response to the phase change $d\phi$ is derived as follows.

$$P(\phi) = |T(\phi)|^2 = \frac{2y^2(1 - \cos\phi)}{y^4 + 1 - 2y^2 \cos\phi}. \quad (2)$$

$$\frac{d}{d\phi} P(\phi) = \left\{ \frac{y(y^2 - 1)}{y^4 + 1 - 2y^2 \cos\phi} \right\}^2 \cdot 2 \sin\phi. \quad (3)$$

Figure 2(a) and 2(b) show the calculated results of the above formulas using the power coupling efficiency $1 - y^2$ in the coupling region as a parameter. In the calculations, ϕ varies from $-\pi$ to $+\pi$, corresponding to a full range of the FSR. As the narrow black curve in Fig. 2(a) shows, $P(\phi)$ dips steeply for relatively small $1 - y^2$ ($= 10\%$) at the resonant wavelength, or $\phi = 0$. Because of this slope, a tiny change in the refractive index can cause a large change in $P(\phi)$, as the two peaks of opposite sign indicate in Fig. 2(b). However, a large $dP/d\phi$ is available at limited ranges of ϕ , as shown in the graph, corresponding to a narrow wavelength bandwidth in the operation of the SRR-SSM. If $1 - y^2$ is relatively large ($= 40\%$) and the resonance is weak, it is possible to widen the range of ϕ , as the narrow red curve in Fig. 2(a) shows. However, the peak value of $dP/d\phi$ becomes smaller, as shown in Fig. 2(b). This trade-off between modulation efficiency and optical bandwidth can be a drawback in real applications. It is clear in Eqs (2) and (3) that no other design parameter can be changed to avoid this trade-off. One might think to change R and thus ϕ , but this yields roughly the same results as $1 - y^2$. The transfer function of N cascaded RRs in this configuration without an interferometer is obtained as the N th power of that of a single RR, or T^N . As the bold red curve in Fig. 2(a) shows, although the bottom of the $P(\phi)$ curve becomes wide, the slope of the curve is rather moderate between the on- and off-resonance conditions. Therefore, a wider but smaller $dP/d\phi$ is obtained compared with the single RR case, as shown in Fig. 2(b). It is possible to design a steep slope at the edge of the resonance band using coupled RRs. However, the bandwidth of $dP/d\phi$ would remain narrow in any case. In this type of modulator without an interferometer, modulation occurs at the edge of the resonance band when the spectrum shifts. Therefore, it is less important to make the resonance band wide and deep by using a number of cascaded or coupled RRs. Regardless of the number and configuration of the RRs, the shift in the spectrum ($\Delta\lambda$) is given as $\Delta\lambda = (\lambda/n) \cdot \Delta n$, where λ , n , and Δn are the wavelength of light in vacuum, refractive index of the waveguide, and induced change in n , respectively.

2.2 CRR-MZM

Next, we examined the CRR-MZM, in which the phase change of the transfer function of the RRs is used instead of the amplitude change. Propagation loss in the ring waveguide is not necessary and is ideally zero. Therefore, we substitute $x = 1$ in Eq. (1). Although some propagation loss always accompanies RRs owing to the radiation along the bent waveguide and scattering from the sidewall roughness of the waveguide, the impact of these factors was experimentally investigated and is described later in this paper. With $x = 1$, the phase of the transmitted light of a single RR (Φ) and its response to a small change in the RT phase (ϕ) are derived as follows.

$$\tan \Phi(\phi) = \frac{(y^2 - 1) \sin \phi}{2y - (1 + y^2) \cos \phi}, \text{ where } \Phi = -\arg \{T(\phi)\}. \quad (4)$$

$$\eta = \frac{d}{d\phi} \Phi(\phi) = \frac{1 - y^2}{(1 + y^2) - 2y \cos \phi}. \quad (5)$$

In Eq. (5), η exactly represents the enhancement in the phase modulation of the RR due to the effect of the resonance and therefore is the principal parameter used to describe an RR-based phase modulator [28]. If there is no resonance and $y = 0$, $\eta = 1$.

Figure 2(c) and 2(d) show the values of Φ and η calculated by the above formula for the same parameter sets as in Fig. 2(a) and 2(b) except for x . As the narrow black curve shows, Φ changes rapidly around $\phi = 0$ because of the resonance with relatively weak coupling ($1 - y^2 = 10\%$). Accordingly, a large η is observed at the resonance. In this case, the range of ϕ with this large η is very narrow, as Fig. 2(d) shows. By comparing the narrow red curves ($1 - y^2 = 40\%$) with the narrow black curves in Fig. 2(d), we can observe the trade-off between the peak value of the enhancement factor η and the bandwidth, similar to the case of Fig. 2(a) and 2(b). Unlike those cases, however, when a number of RRs are cascaded in an APF configuration, like those on each arm of the MZI in Fig. 1(c), it is possible to obtain a wider bandwidth while maintaining the large η . The bold red curve in Fig. 2(d) confirms this design with the parameters $1 - y^2 = 40\%$ and $N = 5$. The curve has roughly the same peak value of η as the narrow black curve and the same bandwidth as the narrow red curve. As mentioned above, the transfer function of N cascaded RRs is calculated as the N th power of that of a single RR, or T^N , and accordingly the phase of T^N is given by multiplying Φ for $N = 1$ by N . Thus, it is straightforward to increase η by cascading a number of RRs while maintaining the bandwidth of the RRs. Using a change in phase rather than amplitude enables the use of the inside of the resonance band of RRs and the accumulation of phase changes by cascading the RRs. The MZI is needed to convert the phase change into an intensity change.

The FWHM for η is given in wavelength by approximating the resonance as a simple Lorentzian using temporal coupled mode theory [27],

$$\Delta\lambda_{FWHM} = \frac{\lambda^2}{2\pi n_g} \frac{1 - y^2}{2\pi R}, \quad (6)$$

where n_g is the group index of the ring waveguide. In addition, the peak of η is given as

$$\eta_{MAX} = \frac{1 + y}{1 - y}, \quad (7)$$

at the resonant wavelength with $\phi = 0$ in Eq. (6). Equations (7) and (8) yield the design fundamentals for the CRR-MZM. First, the minimum bending radius R should be used unless the radiation loss becomes significant. When a small R is used, the bandwidth $\Delta\lambda_{FWHM}$ becomes large, whereas η_{MAX} remains constant. Next, y should be determined to obtain sufficient $\Delta\lambda_{FWHM}$ for the specific application. With the resulting y , the phase change of a single RR ($\Delta\phi$) for a given index change Δn is given as

$$\Delta\Phi = \frac{1 + y}{1 - y} \frac{2\pi(2\pi R)}{\lambda} \Delta n. \quad (8)$$

Finally, the number of cascaded RRs (N) is determined to obtain an adequate overall phase change ($N \cdot \Delta\Phi$) for the required modulation depth. Note that as long as y is less than 1, the presence of the RRs ensures some enhancement with $\eta_{MAX} > 1$, regardless of the other parameters.

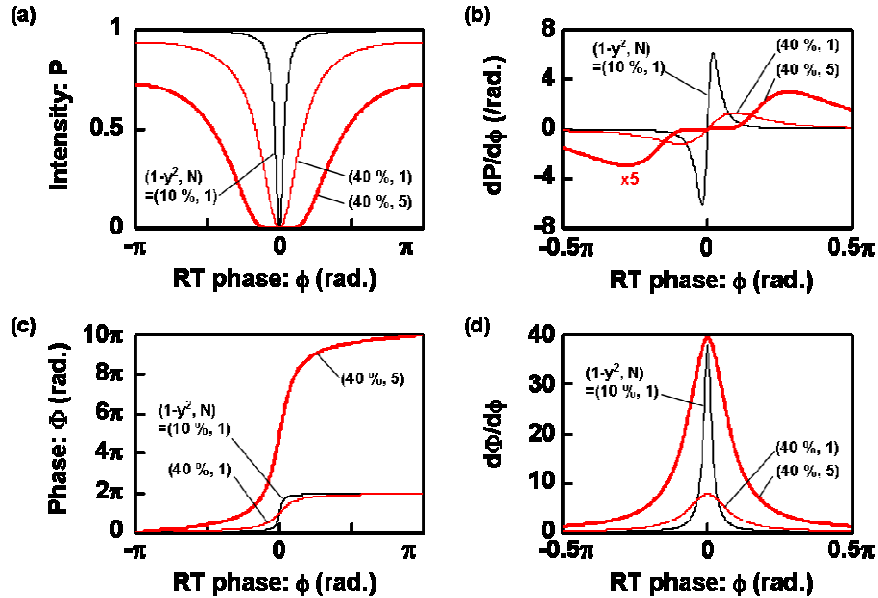


Fig. 2. Calculated response of single RR and five cascaded RRs as a function of RT phase ϕ . $1-y^2$ is coupling efficiency of coupling region in RRs. A power of $1-y^2$ is transferred from bus to ring waveguide in the coupling region. N corresponds to the number of RRs cascaded. (a) Intensity P . (b) Sensitivity of P to changes in ϕ . (c) Phase Φ . (d) Sensitivity of Φ to changes in ϕ . (a) and (b) are calculated for critical coupling, whereas (c) and (d) are calculated for the lossless case.

3. Optimization of ring resonators

We experimentally investigated the transmission properties of single or cascaded RRs with different structural parameters in order to optimize them for CRR-MZMs. Passive waveguides having no dopants or electrodes were used without an interferometer.

Figure 3(a) and 3(b) show the cross section and pattern of the waveguide used in the experiments, respectively. As Fig. 3(a) shows, all of the waveguides were made of silicon on a buried oxide layer that had the cross section of a conventional rib waveguide [4,6–14]. We formed the RRs in a racetrack shape, although they were modeled as a simple circle in the previous section, as shown in Fig. 3(b). Both configurations are referred to as “RR” in this paper. We used the racetrack shape because it is suitable for obtaining relatively large coupling between the bus and the ring (or racetrack) waveguide without significant loss. We assign the parameter L_c to the length of the coupling region made of straight waveguides. The parameter R indicates the bending radius of the racetrack. The gap between waveguides in the coupling section was about 150 nm throughout the rest of this paper. We fabricated a single RR and 10 cascaded passive RRs with various values of R and L_c . All of the RRs connected to the same bus waveguide had the same R and L_c throughout the rest of this paper. We measured the intensity and group delay (GD) spectra of the RR transmission. We used the modulation phase shift method to measure the GD spectrum. Transverse electric polarization was used in the measurements.

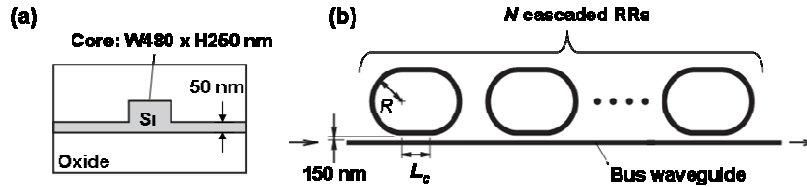


Fig. 3. Schematic of RRs used in experiments. (a) Cross section of waveguide. (b) Waveguide pattern and definition of parameters.

Figure 4 shows the measured intensity and GD spectra of a single RR with $L_c = 5.0 \mu\text{m}$ and $R = 2.5, 4.0,$ and $7.2 \mu\text{m}$. The spectra show a series of dips and peaks with the same FSR as shown in Fig. 4. We extracted FSRs from the measured spectra in Fig. 4 and calculated the group index of the waveguide, as $n_g = \lambda^2 / (\text{FSR} \cdot 2\pi R)$. All the calculated n_g were equal to 4.1 for RRs with $R = 2.5, 4.0,$ and $7.2 \mu\text{m}$. This value of n_g gave close agreement with its expected value for the rib-waveguide with the cross section of Fig. 3(a).

The nearest peaks to 1550 nm in the GD spectra were fitted by a Lorentzian function to derive the FWHM and peak value from the noisy spectrum, as shown in Fig. 5. The resulting values are indicated in the figures, where the peak GDs were converted to n_{g_eff} by dividing them by the perimeter of the RR and then multiplying by the vacuum velocity of light. These n_{g_eff} values represent the factor by which light is slowed in the RRs and correspond to η in the previous section. As seen in Fig. 5, the RRs having a smaller R had a larger n_{g_eff} and FWHM, both of which are desirable for a CRR-MZM. The reason for this dependence of the RRs is explained as follows. When R decreased, the loss of the propagating light per round-trip increased due to the large radiation loss with the small bending radius of the waveguide. Since all the RRs presented in our paper are used in over-coupling regime, the RR approached to the critical coupling with increase of the round-trip loss [26,29]. When RR moves to the critical coupling from the over-coupling regime, the intensity and group delay of the transmitted light are expected to decrease and increase, respectively [29]. This is the reason why RRs having a smaller R had a larger n_{g_eff} in our experiments. As for FWHM, although the slight increase of n_{g_eff} for smaller R made the spectrum narrower, the decrease of R broadens the resonance due to the large FSR. The FWHM is determined by the balance of these two dependencies. As a result, measured FWHM increased for RRs with smaller R .

The optical loss is another important characteristic of the RRs. In principle, a large GD is accompanied by a large loss because light propagates effectively on the long waveguide. Therefore, the loss per unit GD of the RRs should be compared to evaluate their excess loss. In Fig. 6, we plotted the GDs as a function of the loss for each wavelength in a single peak and dip, which were those nearest to 1550 nm in the spectra in Fig. 4. The slopes of the plots represent the excess loss of the RRs. The RRs with a smaller R clearly had a larger excess loss for a constant GD. In a CRR-MZM, the loss is multiplied by the number of cascaded RRs. Consequently, R should be larger than $4.0 \mu\text{m}$, at least, in order to obtain a reasonably small optical loss. We chose the RR with $R = 7.2 \mu\text{m}$ for our experiments.

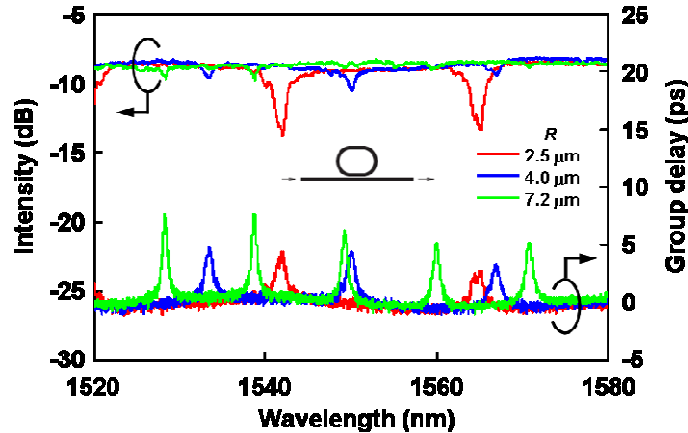


Fig. 4. Transmission spectra in intensity and GD of single RR with $L_c = 5.0 \mu\text{m}$ and $R = 2.5, 4.0,$ and $7.2 \mu\text{m}$.

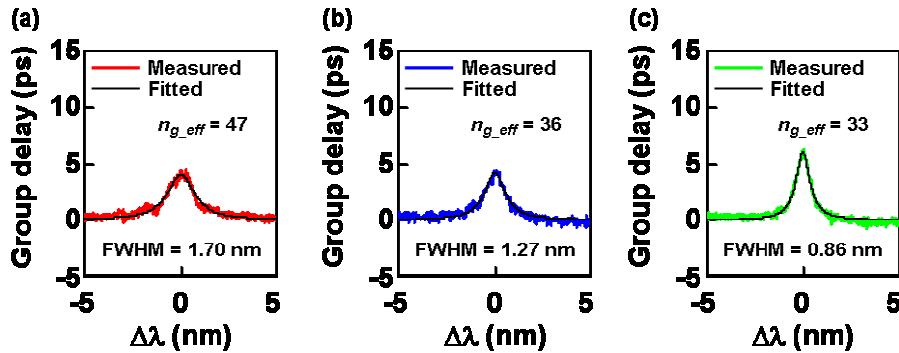


Fig. 5. Single peaks nearest to 1550 nm in GD spectra in Fig. 4. Measured curves are fitted by a Lorentzian function. (a) $R = 2.5 \mu\text{m}$. (b) $R = 4.0 \mu\text{m}$. (c) $R = 7.2 \mu\text{m}$.

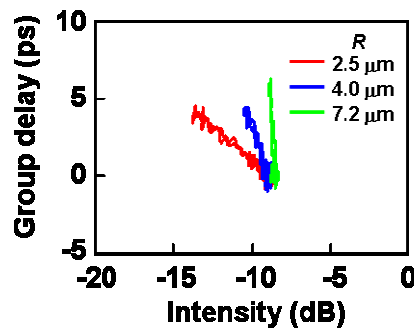


Fig. 6. GD-intensity plot of single peak nearest to 1550 nm in the spectra in Fig. 4.

Next, we investigated the dependence of the RR transmission properties on L_c . Figure 7 shows the measured transmission spectra in intensity and GD of RRs with $R = 7.2 \mu\text{m}$ and $L_c = 2.5, 5.0,$ and $7.5 \mu\text{m}$. The RRs having smaller L_c values had a larger GD at the resonant wavelength but a narrower wavelength bandwidth. Figure 8 shows the single peaks and dips of intensity and group delay, respectively, nearest to 1550 nm. We fitted those curves by analytical formula derived from Eq. (1), as shown by black solid curves in Fig. 8 [29]. The measured curves were reasonably fitted using the parameters of x and $1-y^2$ indicated in Fig. 8.

In our experiment, $L_c = 2.5, 5.0,$ and $7.5 \mu\text{m}$ correspond to the coupling efficiencies of $1-y^2 = 18, 39, 61\%$.

We derived n_{g_eff} and the FWHM for a single peak in the GD spectra in Fig. 7, in the same way as in Fig. 5. The results are summarized in Fig. 9(a) and 9(b), respectively, for $R = 2.5, 4.0,$ and $7.2 \mu\text{m}$. The trade-off between n_{g_eff} and the FWHM is noticeable, as mentioned in section 2. For $R = 7.2 \mu\text{m}$, an n_{g_eff} value of greater than 81 was achieved at $L_c = 2.5 \mu\text{m}$, at the expense of a narrow bandwidth of about 0.36 nm . In contrast, a FWHM of about 1.4 nm was obtained at $L_c = 7.5 \mu\text{m}$, although n_{g_eff} was limited to about 17 in this case. Unlike the dependence on R , we found that L_c did not significantly affect the extra loss of the RRs. Figure 10 shows the GD-intensity plot for RRs with $R = 7.2 \mu\text{m}$ and $L_c = 2.5, 5.0,$ and $7.5 \mu\text{m}$ based on the spectra in Fig. 7. The slopes remain constant regardless of L_c . The reason for this dependence is explained as follows. η in Eq. (5) decreased with increase of L_c via the change of $1-y^2$. η represents the equivalent number of the round trips that light makes at each RR. Therefore, the total propagation loss and GD that light experiences at each RR are proportional to $\eta \cdot \alpha \cdot (2\pi R)$ and $\eta \cdot (n_g/c_0) \cdot (2\pi R)$, respectively, in over-coupling regime. Thus, the change of η did not give a large impact on the ratio between the total loss and GD. Note that α kept almost constant, as calculated from the x in Fig. 8 and the round-trip length of the RRs.

Finally, the transmission spectra of 10 cascaded RRs with $R = 7.2 \mu\text{m}$ and $L_c = 2.5, 5.0,$ and $7.5 \mu\text{m}$ are shown in Fig. 11. The red curve exhibits a few subpeaks associated with each of the large peaks. For RRs with $L_c = 2.5 \mu\text{m}$, the resonance of each RR was so sharp that the FWHM was smaller than the fluctuations of the resonant wavelengths of the RRs owing to non-uniform fabrication. In this case, the peak value of the GD and its bandwidth are uncontrollable; therefore, this design using RRs with too strong resonance should be avoided in a CRR-MZM. The other two devices exhibited a series of single large peaks and dips in the intensity and GD spectra, respectively. They had a similar FWHM to those of a single RR with the same parameters, whereas the peak GD values were several times larger than those in a single RR. This confirms the design concept of the CRR-MZM mentioned in section 2. RRs with weak resonance are used to obtain a relatively large resonant bandwidth. The small GDs for each RR were accumulated to obtain a large total GD. In this paper, we chose $L_c = 7.5 \mu\text{m}$ and fabricated a CRR-MZM with $R = 7.2 \mu\text{m}$ and $N = 10$ to demonstrate efficient yet wide-wavelength-band operation.

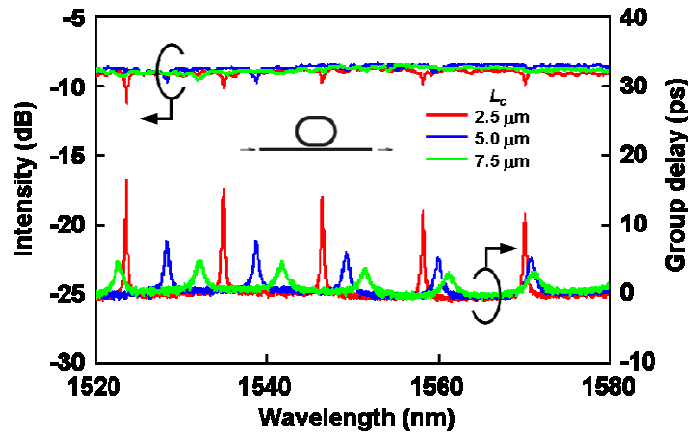


Fig. 7. Transmission spectra in intensity and GD of single RR with $R = 7.2 \mu\text{m}$ and $L_c = 2.5, 5.0,$ and $7.5 \mu\text{m}$.

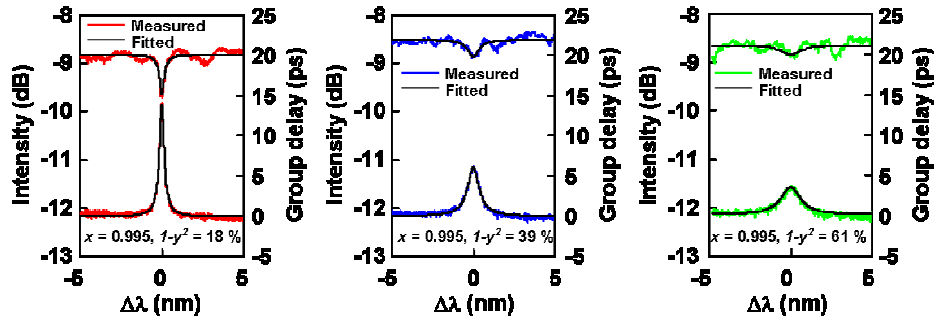


Fig. 8. Single peaks nearest to 1550 nm in intensity and GD spectra in Fig. 7. Measured curves of spectra for intensity and group delay derived from the Eq. (1), with the parameters of x and y . The values of x and y ($1-y^2$) used in the fittings are indicated in each graph. (a) $L_c = 2.5 \mu\text{m}$. (b) $L_c = 5.0 \mu\text{m}$. (c) $L_c = 7.5 \mu\text{m}$.

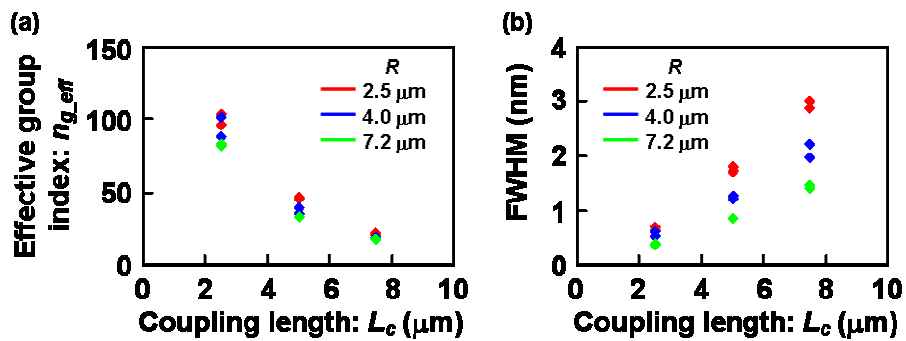


Fig. 9. Summary of GD characteristics of RRs with different values of R and L_c derived from single peak of GD nearest to 1550 nm in the spectra. Two samples were measured and analyzed for each combination of R and L_c . (a) Effective group index ($n_{g,eff}$) and (b) FWHM.

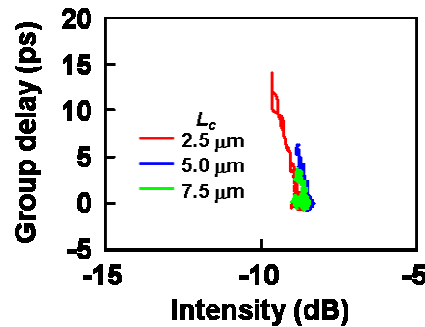


Fig. 10. GD-intensity plot of single peak nearest to 1550 nm in the spectra in Fig. 7.

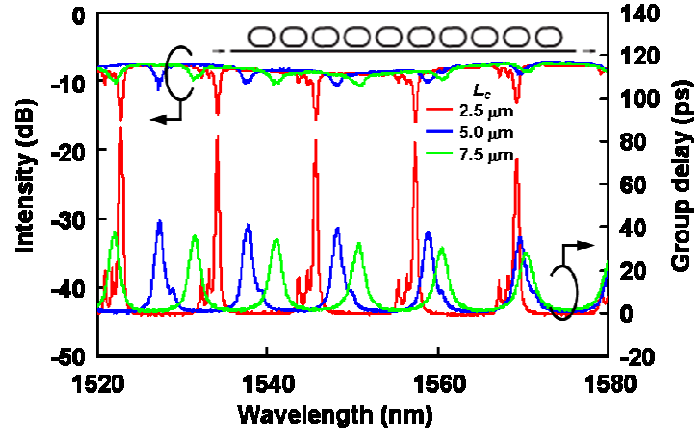


Fig. 11. Transmission spectra in intensity and GD of 10 cascaded RRs with $R = 7.2 \mu\text{m}$ and $L_c = 2.5, 5.0, \text{ and } 7.5 \mu\text{m}$.

4. Fabricated device structure

In this section, we describe the structure of the CRR-MZM, which was fabricated and measured in the experiments presented in the rest of this paper. Figure 12(a) is a microscope photograph of the fabricated CRR-MZM. An MZI was formed by using two 2×2 multi-mode interference (MMI) couplers on a silicon-on-insulator substrate. Ten cascaded RRs were loaded on each arm of the interferometer. The structure of the RRs is shown schematically in detail in Fig. 12(b) and 12(c). All of the waveguides were made of silicon on a buried oxide layer. The geometry of the cross section of the waveguide was the same as that in Fig. 3(a). As Fig. 12(c) shows, the slabs on both sides of the core of the waveguide were highly p- and n-doped to about $10^{19} / \text{cm}^3$, and the side of the core and the part of the slabs adjacent to the core were lightly p- and n-doped to about $6\text{--}7 \cdot 10^{17} / \text{cm}^3$. Those lightly doped regions shared a border at the center of the core after the implantations. However, the dopants were thermally activated by annealing at $1000 \text{ }^\circ\text{C}$, for 15 min. for p-type (B^+) and for 20 min. for n-type (P^+), respectively, and they were suspected to diffuse from the original region to the opposite side of the core beyond the center line. This diffusion made the net-doping level in the center of the core small. Therefore, we assumed that the CRR-MZM behaved much like pin diodes rather than pn diodes. Aluminum electrodes were formed inside and outside of each RR along the ring on the highly doped parts of the slabs. In the operation of this CRR-MZM, free carriers such as electrons and holes are injected to and extracted from the core of the ring waveguide by applying a voltage between the electrodes on either side of the core. These free carriers change the refractive index of the waveguide via the free-carrier plasma (FCP) effect, and thus modulate the light propagating through the RRs.

We fabricated and investigated a CRR-MZM with the parameters of $R = 7.2 \mu\text{m}$ and $L_c = 7.5 \mu\text{m}$ as a consequence of the optimization of RRs described in the previous section. With these parameters, the total length of the active waveguide was $527 \mu\text{m}$ per arm. This length was calculated as $N \cdot (2\pi R + L_c) = 10 \cdot (2\pi \cdot 7.2 + 7.5) = 527 \mu\text{m}$. Note that the bus waveguides and the outside of the RRs in the coupling region were not doped as shown in Fig. 12(b). Those parts did not contribute modulation of light and were excluded in the calculation of the active length.

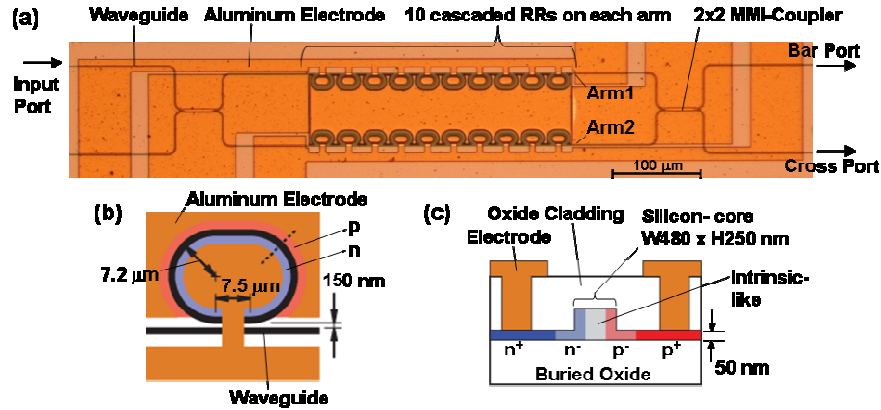


Fig. 12. Fabricated CRR-MZM. (a) Microscope photograph of top view. (b) Schematic view of one of cascaded RR in (a). (c) Schematic of cross section of dotted line in (b).

5. Characteristics of CRR-MZM

In this section, the measured characteristics of the fabricated CRR-MZM with $L_c = 7.5 \mu\text{m}$, $R = 7.2 \mu\text{m}$, and $N = 10$, are presented.

5.1 Transmission properties

First, we measured the transmission spectrum of the CRR-MZM. For comparison, the results of a reference waveguide and standard MZM are also shown. The reference waveguide was a single straight rib waveguide without an interferometer, RRs, dopants, or an electrode, and it had the same cross-sectional geometry as in Fig. 12(c). The standard MZM had a straight non-resonant phase shifter on each arm of the MZI with a length of $500 \mu\text{m}$ and a cross section identical to that in Fig. 12(c). All three devices were fabricated on the same silicon-on-insulator wafer and underwent the same wafer process. Since they were on the same test chip, in the measurements, light traveled the same physical lengths from one of the facets of the chip to the other one, for all the three devices. In the MZM measurements, we consistently used one specific optical port to input the lightwave on one side of the two facets while using either of the two ports on the opposite facet alternately to output the lightwave. We defined the bar and cross ports on the output facet as shown in Fig. 12(a).

In Fig. 13, the red and blue curves for the two MZMs were formed by summing the two spectra obtained from the bar and cross ports to eliminate the effect of the built-in phase difference between the two arms of the MZI and observe the intrinsic loss of the devices. The transmission of the two MZMs decreased with wavelength, whereas that of the reference waveguide (black curve) increased slightly. This difference is attributed to the wavelength dependence of the MMI couplers. As intended, the fabricated CRR-MZM showed periodic dips. No splits due to the distribution of resonant wavelengths were observed inside each dip.

For the two MZMs, the decrement from the black curve indicates the on-chip IL of the modulators at each wavelength. The CRR-MZM had an on-chip IL of less than 0.5 dB as the maximum transmission obtained at the off-resonant wavelengths of the RRs around 1550 nm, as shown in Fig. 13(a). This small loss is reasonable because, in this case, light propagates effectively shorter doped waveguide in RRs, shorter than its physical length. In fact, $\phi = \pm \pi$ yield enhancement factor η smaller than 1 for $y > 0$ in Eq. (5). However, this means we can expect only small modulation of light at those wavelengths. As is obvious from the discussion in section 2, the maximum modulation of light is expected at the bottom of the dips in the spectrum of the CRR-MZM. At the bottom of the dip nearest to 1550 nm, the CRR-MZM had the additional 4.0-dB loss from the aforementioned 0.5-dB IL. This 4.5 dB loss in total includes the loss due to the MMI couplers, dopants, and RRs, and was not much larger than those of FCP-based silicon modulators [3–18].

We next, compared the CRR-MZM with the standard MZM, both of which had about the same active lengths. The transmission of the CRR-MZM was larger than that of the standard MZM at off-resonant wavelengths. This is because light propagates 500-nm long doped phase shifter for the standard MZM regardless of the wavelength, whereas it propagates effectively shorter doped waveguide in RRs at those wavelengths for the CRR-MZM as mentioned above. On the other hand, at the bottom of the dip nearest to 1550 nm, the transmission of the CRR-MZM was 3.5 dB smaller than that of the standard MZM, as indicated by the arrow in Fig. 13(a). At this wavelength, light propagates RRs effectively many times, causing this 3.5-dB additional loss for the CRR-MZM. At the same time, the CRR-MZM showed the enhancement of modulation efficiency at this wavelength, as described in the next part of this paper. This loss was rather small if we consider it as the cost for the enhancement of the modulation.

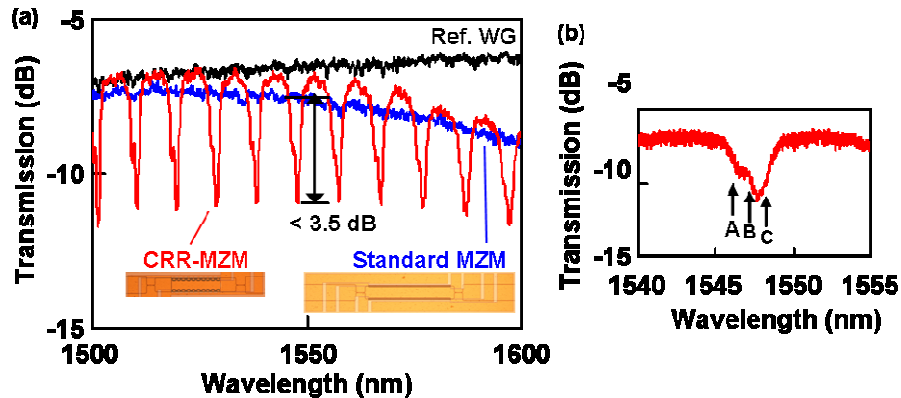


Fig. 13. (a) Measured transmission spectra of reference single passive waveguide (black), standard MZM (blue), and CRR-MZM (red). The photographs inside graph show device parts of test chip. (b) Close-up of single dip in the spectrum of the CRR-MZM. Arrows indicate wavelengths at which 10-Gb/s eye diagrams shown in Fig. 17 were measured.

5.2 Modulation enhancement

Next, we evaluated the enhancement of the modulation efficiency of the CRR-MZM compared with the standard MZM. We used the FCP effect to modulate the refractive index of the silicon waveguide by injecting electrons and holes into the core. When carriers are injected, heat is generated, which has the opposite effect on the index change, reducing the overall modulation at frequencies typically smaller than 1 MHz and at DC. On the other hand, the dynamics of the injected carriers limit the modulation efficiency of the FCP effect above 1 GHz. A frequency range of 10–100 MHz is suitable for eliminating the effect of heat and the carrier dynamics, and to evaluate only the effect of the RRs on the modulation efficiency. We conducted a 100-Mb/s large signal modulation experiment using the fabricated CRR-MZM and standard MZM to compare their modulation efficiencies. In the measurements, one of the two arms of the MZI was driven by 100-Mb/s random signals with a DC forward bias voltage of 0.9 V. We adjusted the bias current of the opposite arm to obtain the same extinction ratio (ER) between the output signals from the bar and cross ports. In this configuration, we changed the amplitude of the driving signals and found the values at which the ER became about 3 dB.

The results are summarized in Table 1. Because modulation with a forward bias voltage is highly efficient, the voltage amplitude needed to obtain a 3 dB ER was as small as $121\text{ mV}_{\text{pp}}$ on average for the standard MZM. For the CRR-MZM, the amplitude was further reduced to $26.2\text{ mV}_{\text{pp}}$ owing to the enhancement caused by the RRs. We calculated the enhancement of the modulation efficiency taking the difference in the active length into account, as follows:

$$\frac{121 \text{ mV}_{pp}}{26.2 \text{ mV}_{pp}} \cdot \frac{500 \mu\text{m}}{527 \mu\text{m}} = 4.4$$

This factor means we can obtain a reduction of 4.4 times in the driving voltage compared to that of a standard MZM by using a CRR-MZM with the same total active length, if only the cross sections of the phase modulators are the same. The power consumption of the modulator is proportional to CV^2 , where C is the total capacitance of the modulator, and V is the amplitude of the driving voltage. From this formula, a reduction in V by a factor of 4.4 reduces the power consumption by 19 times, which is significant in most applications.

This enhancement factor corresponds to n_{g_eff}/n_g , using the definitions of n_{g_eff} and n_g in earlier sections. The measured n_{g_eff} was 17 for a passive RR with $R = 7.2 \mu\text{m}$ and $L_c = 7.5 \mu\text{m}$, as in the previous section, and n_g for the rib waveguide was about 4. Using these values, n_{g_eff}/n_g was calculated to be 4.25, which agrees well with the factor of 4.4.

Table 1. Performance Comparison between CRR-MZM and Standard MZM in 100 Mb/s-modulation Experiments

Device type	Operating wavelength	Driving arm	Driving voltage	Dynamic ER	
				Bar port	Cross port
CRR-MZM	1547.68 nm	1	27.7 mV	3.00 dB	3.19 dB
		2	24.6 mV	3.06 dB	2.93 dB
Standard MZM	1550.00 nm	1	116 mV	2.71 dB	3.36 dB
		2	127 mV	3.03 B	2.98 dB

The DC bias voltage of the driving arm was kept at + 0.9 V, whereas that in the opposite arm (not driven) was adjusted to obtain the identical dynamic ER between the bar and cross ports.

5.3 10-Gb/s large-signal modulation experiments

Finally, we performed large-signal modulation experiments at 10 Gb/s using the fabricated CRR-MZM. Figure 14(a) illustrates the experimental setup. We kept the diodes in the RRs at a forward bias during the experiments to operate the modulator in the injection mode. The 3-dB bandwidth of the modulator was typically smaller than 1 GHz; in this situation, pre-emphasis signals are typically used to compensate for the slow dynamics of the injected carriers [4,7,9,13,14]. For this purpose we used in-line-type differentiators (Picosecond Pulse Lab, Model 5206, passive impulse forming network) that output the derivative of the input signals with a compensating slope of + 20 dB/decade as the frequency increases. Thus, standard non-return zero signals from a pulse-pattern-generator were converted to pre-emphasis signals of the form shown in Fig. 14(b). The peak-to-peak amplitude of the voltage was 1.5 V_{pp} monitored after the amplifier. Two such voltage waveforms at opposite polarities were applied to each of the two arms of the MZM to drive it in a push-pull configuration. The forward bias voltages were adjusted to around + 0.9 V to obtain the desired phase difference and added to the high-speed signals using bias-tees.

Figure 14(c) shows the optical output waveform measured from the bar port of the modulators. The wavelength of the input light was 1547.68 nm, which corresponded to the bottom of the dip in the transmission spectrum. We obtained clear openings, as shown in the eye diagram, with a dynamic ER of 3.0 dB. We confirmed the same ER in the output waveform from the cross port, which indicates that the phase difference of the interferometer remained at the quadrature point during operation. The voltage amplitude of 1.5 V_{pp} , which is relatively small for a silicon-based modulator, was achieved because of the enhanced modulation efficiency of the RRs. As mentioned in section 5.1, our CRR-MZM had an on-chip optical loss of 4.5 dB without DC bias or RF signals, compared with the reference waveguide at the resonant wavelength. During 10-Gb/s operation with DC bias and RF signals, the optical loss further increased by 4.8 dB for the average output power from the bar port. This additional loss included 3-dB loss due to the power distribution between bar and cross ports; we set the MZI at quadrature phase balance during the operation. Thus, 4.8-3.0 = 1.8 dB was the loss due to the injected carriers during the 10-Gb/s operation with forward bias voltage. The total on-chip loss of the CRR-MZM during 10-Gb/s operation was 4.5 + 4.8 =

9.3 dB for the average output power from one of the two ports, including all kinds of excess loss from the reference waveguide. As for power imbalance between the two arms, since both of the two arms were equally DC-biased around 0.9 V, the increase of the loss due to the injected carrier was largely balanced between the two arms and expected not to deteriorate ER.

We acquired optical eye diagrams at different wavelengths around 1547.68 nm. We changed the bias voltages slightly to maintain the phase balance at the quadrature point and obtain the same ER at both ports. Figure 15(a) and 15(b) show the ER of the measured eye diagrams and the optical IL, defined as the decrement of the average output power from that of the input continuous lightwave including optical coupling loss, respectively. The ER and IL decreased as the wavelength shifted from the maximum resonance because the light propagates for an effectively smaller length as the enhancement factor decreases. The ER and IL both had roughly inversed dependences of transmission spectrum in Fig. 13(b) against the lateral axis, as expected. If we define the bandwidth as the wavelength range in which the ER is more than half of the maximum, it is estimated to be about 2 nm.

It is preferable that both the ER and IL remain constant when the input wavelength changes. We investigated the possibility of this type of operation for the CRR-MZM by changing the phase balance of the interferometer during 10 Gb/s operation. For an MZI, it is possible to obtain a larger ER at the expense of a larger extra IL when the DC phase difference between the arms approaches π from the quadrature point. On the basis on this idea, we adjusted the bias voltages so that the ER of the eye diagram from the bar port remained 3 dB. The resulting ER and IL are shown in Fig. 16(a) and 16(b), respectively. ERs of 2.9–3.1 dB were obtained at a wavelength range of 2 nm, while the variation in the IL remained within 1 dB. A constant IL was obtained because the increase in the extra IL was balanced by the reduction in the propagation loss of the RRs as the input wavelength deviated from the maximum resonance. In this type of operation, the maximum range of the phase difference to be adjusted by DC bias voltage is less than $\pi/2$. For our CRR-MZM, the voltage change less than 0.1 V would be sufficient for the phase adjustment of $\pi/2$, as estimated from the results in Table 1, if the influence of heat generation is negligible. This change of the voltage adds the extra loss of 1 to 2 dB to the arm around 0.9 V. Such small imbalance in power would not cause serious degrade in ER in most applications. Although our CRR-MZM suffered from heat generation at DC operation, and needed more change in bias voltage to adjust the phase balance, ER as large as 3 dB was obtained as shown in Fig. 16(a) even in this case.

Figure 17 shows the optical waveforms at the three wavelengths indicated in Fig. 13(b). We successfully obtained clear identical eye diagrams in a wavelength range of 2 nm, which is about 20 times larger than those expected for SRR-SSMs. Low-voltage operation of the CRR-MZM in a relatively wide wavelength range was achieved by its flexible design concept. If RRs having a stronger resonance are used, a smaller driving voltage is possible in a narrower wavelength band, as presented in an earlier paper [14], using the same active length of the modulator. Alternatively, cascading more RRs is another way to reduce the driving voltage while maintaining the same wavelength bandwidth of the RRs. Note that the cross section of the waveguide has not been optimized for use as a phase modulator in our experiments. Further improvements of CRR-MZMs are expected if the cross section of the phase modulator is used with optimized doping profiles and geometry, as reported in other works.

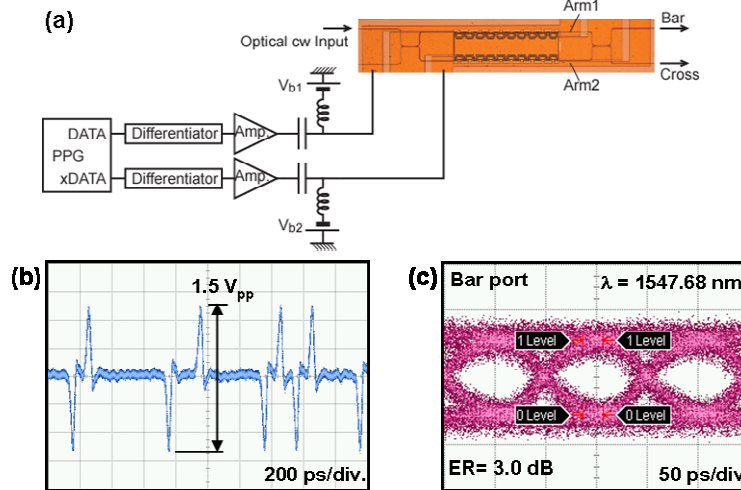


Fig. 14. 10-Gb/s large-signal modulation experiment using fabricated CRR-MZM. (a) Experimental setup. (b) Driving voltage waveform. (c) Eye diagram of optical output.

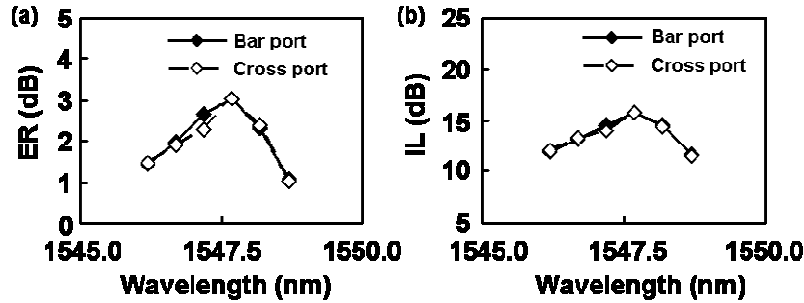


Fig. 15. Dependence of (a) ER and (b) IL on input wavelength in 10-Gb/s modulation experiments. Phase balance between the two arms was adjusted to obtain the same ER at the bar and cross ports.

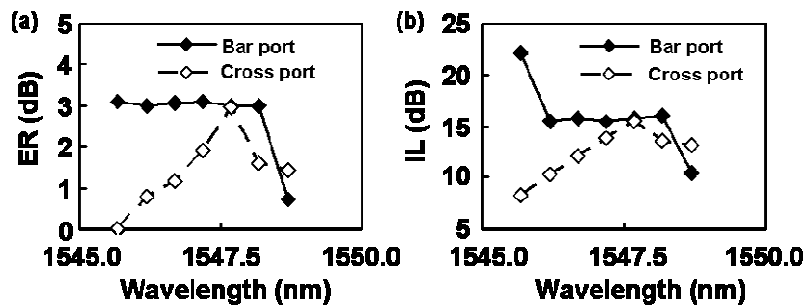


Fig. 16. Dependence of (a) ER and (b) IL on input wavelength in 10-Gb/s modulation experiments. Phase balance between the two arms was adjusted to obtain a constant ER from the bar port.

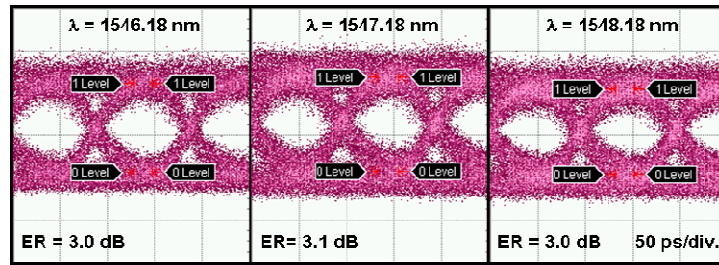


Fig. 17. 10-Gb/s eye diagrams of fabricated CRR-MZM in wavelength range of 2 nm. Input wavelengths were those indicated by arrows in Fig. 13(b).

6. Conclusion

We investigated a CRR-MZM for enhanced modulation efficiency at a wider optical bandwidth. We demonstrated the advantage of the CRR-MZM over a conventional SRR-SSM in design capability by analytical calculations; it is possible to increase the total modulation efficiency of the CRR-MZM for a given refractive index change by cascading a number of RRs while retaining a relatively broad resonance of the RRs.

On the basis of our analysis, we experimentally optimized the structural parameters of the RRs for a CRR-MZM using a silicon rib waveguide having a conventional geometry. Although RRs with a small bending radius showed better GD performance, the impact on the propagation loss was significant. Changing the coupling efficiency exhibited an ordinary trade-off between the GD and its bandwidth with a constant slope between the GD and the loss. Another restriction for the design of the RRs in the CRR-MZM was identified: the bandwidth of each RR should be large enough to accommodate fluctuations in its resonant wavelength due to non-uniform fabrication in order to avoid peak splits.

Using 10 cascaded RRs with optimized parameters, we fabricated a CRR-MZM on a silicon-on-insulator substrate and characterized it by various methods. We compared it with a standard non-resonant MZM having the same active length as the CRR-MZM. The modulation efficiency of the CRR-MZM was enhanced by a factor of 4.4 at the expense of additional loss of less than 3.5 dB at the maximum resonance wavelength. 10-Gb/s operations were successfully demonstrated using the CRR-MZM with a voltage amplitude of $1.5 V_{pp}$ in a wavelength range of 2 nm. The results verified the capability of CRR-MZMs to realize tailored performance in terms of modulation efficiency and optical bandwidth.